Novel linear analysis for a gyrotron oscillator based on a spectral approach

J. Genoud,[1, a)] T. M. Tran,[1] S. Alberti,[1] F. Braunmueller,[1] J-Ph. Hogge,[1] M. Q. Tran,[1] W.C. Guss,[2] and R.J. Temkin[2]

[1)]*Swiss Plasma Center, Ecole Polytechnique Fédérale de Lausanne, Station 13, CH-1015 Lausanne, Switzerland.*

[2)]*Plasma Science and Fusion Center, Massachusetts Institute of Technology, Cambridge, MA 02139 USA.*

(Dated: February 8, 2016)

With the aim of getting a better physical insight in linear regimes in gyrotron, a new linear model was developed. This model is based on a spectral approach for solving the self-consistent system of equations describing the wave-particle interaction in the cavity of a gyrotron oscillator. Taking into account the wall-losses self-consistently and including the main system inhomogeneities in the cavity geometry and in the magnetic field, the model is appropriate to consider real system parameters. The main advantage of the spectral approach, compared to a time-dependent approach, is the possibility to describe all the stable and unstable modes, respectively with negative and positive growth rate. This permits to reveal the existence of a new set of eigenmodes, in addition to the usual eigenmodes issued from cold-cavity modes. The proposed model can be used for studying other instabilities such as for instance backward waves potentially excited in gyrotron beam tunnels.

I. INTRODUCTION

Gyrotrons are microwave sources exploiting the cyclotron resonance maser instability to emit radiofrequency waves in the GHz up to the THz frequency range. These devices are mainly used as high power devices for fusion application but also as low power devices, as for instance for DNP-NMR (Dynamic Nuclear Polarization enhanced Nuclear Magnetic Resonance) spectroscopy. The full description of the interaction between the slightly relativistic electron beam and the resonant mode of the cavity requires self-consistent nonlinear models[1–3]. On the other hand, to describe the excitation limits, linear models are appropriate and have already been extensively studied[2–6]. Most of the models that have been used in the past to calculate the self-excitation condition, expressed in terms of a starting current, are not self-consistent[2,5,7–9], in the sense that the empty-cavity longitudinal eigenmode is used. However, the necessity of using a self-consistent model has been discussed in several publications[6,10–13], especially for backward-wave interactions where self-consistent effects are important. The majority of these models are time-dependent, describing the time evolution of the most unstable mode. The model presented in this paper is based on a spectral approach, permitting to study not only the most unstable mode, but also all the stable and unstable modes. In that sense, this approach is a novelty and allows to gain a deeper physical insight on the linear dynamics taking place inside the cavity of a gyrotron oscillator. Moreover, the spectral approach is more convenient than a time-dependent approach for starting-current calculation, requiring less computational resources, as discussed herein. In section II, the model and its derivation is described.

In section III, the numerical implementation is presented. The model validation against different models as well as experimental results is made in section IV. The application of the novel model to two distinct cases for which detailed experimental results exist: a), low power high-quality factor gyrotron and, b) high-power low-quality factor gyrotron, is presented and discussed in section V. Section VI concludes the paper.

II. MODEL DESCRIPTION

The new model is based on the nonlinear model of the code TWANG[14], describing self-consistently the wave-particle interaction for a single transverse $\text{TE}_{m,p}$ mode. Together with its linearization it is described in details in references[6,14,15]. An important point to be stressed is that the amplitude and phase of the rf-field profile were considered to vary on a time-scale much longer than the electron transit-time in previous models[6,14] (in the model presented in this paper and in a new reduced 1D Particle-In-Cell (PIC) model[15], this assumption is relaxed). The equations describing respectively the perpendicular and parallel electron motion for each electrons are

$$\frac{\mathrm{d}\mathcal{P}}{d\hat{z}} = \left(-i\frac{\gamma - s\frac{\Omega_c}{\omega_0}}{p_z} + \frac{s}{2}\frac{\mathrm{d}(\ln B_0)}{d\hat{z}}\right)\mathcal{P}$$
$$+ s(-\gamma F^* + ip_z F'^*)C_0\frac{p_\perp^{2s-2}}{p_z}, \quad (1)$$

and

$$\frac{\mathrm{d}p_z}{\mathrm{d}\hat{z}} = -\frac{C_0}{p_z}\text{Im}(F'\mathcal{P}) - \frac{1}{2}\frac{p_\perp^2}{p_z}\frac{\mathrm{d}(\ln B_0)}{d\hat{z}}. \quad (2)$$

[a)]jeremy.genoud@epfl.ch

Whereas the wave-equation for the wave electric field envelope $F(\hat{z}, \tau)$ is

$$\left(2i\frac{\partial}{\partial \tau} + \frac{\partial^2}{\partial \hat{z}^2} + \kappa_{\|0}^2\right)F = i\mathcal{I}\left\langle C_0 \frac{\mathcal{P}^*}{p_z}\right\rangle, \qquad (3)$$

with the boundary conditions at the beginning $(\hat{z}_{\text{in}})$ and end $(\hat{z}_{\text{out}})$ of the interaction space:

$$\left.\frac{\partial F}{\partial \hat{z}}\right|_{\hat{z}_{\text{in/out}}} = \mp i\frac{k_{\|0}}{k_0}F(\hat{z}_{\text{in/out}}, t). \qquad (4)$$

More general frequency-independent non-reflecting boundary conditions have been recently implemented in the model[16], permitting to extend the validity domain of the model to non-stationary regimes[17,18].

The two normalized variables are the normalized axial position $\hat{z} = \frac{\omega_0}{c}z$ and the normalized time $\tau = \omega_0 t$. ω_0 is a reference frequency herein chosen as the cutoff frequency in the constant radius cavity section and c is the speed of light. $\mathcal{P} = p_\perp^s \exp(-i\Psi)$ is the complex perpendicular momentum, $p_\perp$ and p_z are the perpendicular and parallel electron momentum. Ψ is the slow-timescale electron phase. Other quantities are: γ the electron relativistic factor, Ω_c the non-relativistic cyclotron angular frequency and s the harmonic number. B_0 is the external magnetic field amplitude and $F = \frac{e}{m_e c^2}\frac{s^s}{2^s s!}\frac{E}{k_\perp}$ is the normalized electric field envelope with $F' = \partial F/\partial \hat{z}$ its spatial derivative, e and m_e are the electron charge and mass, respectively. E is the complex electric field and $k_\perp$ is the perpendicular wave number. $k_0 = \omega_0/c$ and $k_{\|0}$ are respectively the reference and parallel reference wave number. In the wave equation, the average of the source term is defined as: $\langle V \rangle = \frac{1}{N}\sum_{j=1}^N V_j$ for N electrons at a given $\hat{z}$ and τ, where V stands for any electron beam dynamical quantity.

The three dimensionless constants C_0, $\kappa_{\|0}$ and $\mathcal{I}$ are given by:

$$C_0 \equiv \left(\frac{k_\perp}{k_0}\right)^s \left(\frac{s\Omega_c}{\omega_0}\right)^{1-s} J_{m-s}\left(k_\perp R_g\right), \qquad (5)$$

$$\kappa_{\|0}^2 \equiv 1 - \frac{k_\perp^2}{k_0^2}\left[1 - (1+i)\left(1 + \frac{m^2}{\nu_{mp}^2 - m^2}\right)\frac{\delta_{sk}}{R_w}\right], \quad (6)$$

$$\mathcal{I} \equiv \frac{eZ_0}{m_e c^2}\frac{I_b}{C_{mp}}\left(\frac{s^s}{2^s s!}\right)^2, \qquad (7)$$

with

$$C_{mp} \equiv \frac{\pi}{2}(\nu_{mp}^2 - m^2)J_m^2(\nu_{mp}). \qquad (8)$$

In these expressions, R_w and R_g are the cavity wall and guiding center radius, J_m is the Bessel function of the first kind of order m and ν_{mp} the pth root of its derivative. Z_0 is the vacuum impedance. I_b is the beam current. The wall losses are taken into account self-consistently in the

wave-equation via a correction factor in the normalized parallel number $\kappa_{\|0}$. $\delta_{sk} = \sqrt{\frac{2}{\omega_0 \mu_0 \sigma}}$ is the skin depth, μ_0 the vacuum permeability and σ the wall conductivity.

In TWANGlin[6], the electron equations of motion have been linearized, considering the electric field as a first order term. The model has been simplified, the rf-magnetic field (proportional to $\text{d}F/\text{d}z$) has been neglected which implies that the perturbed parallel electron momentum $p_{z1} = 0$. Moreover no velocity spread for the electron beam have been considered. The system of $2N + 1$ equations for the N electrons and the wave equation can be reduced to three equations by defining two moments of the electron distribution function $\pi_1(\hat{z}, \tau) = \langle \mathcal{P}_1^* \rangle$, $\pi_2(\hat{z}, \tau) = \langle \mathcal{P}_1 e^{2i\psi_0} \rangle$ and the electric field envelope $F(\hat{z}, \tau)$. Considering an electron distribution function $\mathcal{F}(\mathcal{P}_1, \Psi_0, \hat{z}, \tau)$ depending explicitly on the three dynamic variables $\mathcal{P}_1$, Ψ_0, $\hat{z}$ and the evolution variable τ, the assumption of a constant electric field during the electron transit-time can be relaxed. In this case, the average of the spatial derivative of a function $\mathcal{G}(\mathcal{P}_1, \Psi_0)$ can be expressed as

$$\left\langle \frac{\text{d}\mathcal{G}}{\text{d}\tau}\right\rangle = \frac{\partial}{\partial \tau}\langle \mathcal{G}\rangle + \frac{\partial}{\partial \hat{z}}\langle \mathcal{G}v_z\rangle. \qquad (9)$$

This expression can be derived starting from the phase-space continuity equation:

$$\frac{\partial \mathcal{F}}{\partial t} + \frac{\partial}{\partial \mathcal{P}_1}\left(\mathcal{F}\frac{\text{d}\mathcal{P}_1}{\text{d}t}\right) + \frac{\partial}{\partial \Psi_0}\left(\mathcal{F}\frac{\text{d}\Psi_0}{\text{d}t}\right) + \frac{\partial}{\partial z}(\mathcal{F}v_z) = 0. \qquad (10)$$

For a function $\mathcal{G}(\mathcal{P}1, \Psi_0)$, the average of the time derivative is :

$$\begin{aligned}
\left\langle \frac{\text{d}\mathcal{G}}{\text{d}t}\right\rangle &= \iint \text{d}\mathcal{P}_1 \text{d}\Psi_0 \frac{\text{d}\mathcal{G}}{\text{d}t}\mathcal{F} \\
&= \iint \text{d}\mathcal{P}_1 \text{d}\Psi_0 \left[\frac{\partial \mathcal{G}}{\partial \mathcal{P}_1}\frac{\text{d}\mathcal{P}_1}{\text{d}t}\mathcal{F} + \frac{\partial \mathcal{G}}{\partial \Psi_0}\frac{\text{d}\Psi_0}{\text{d}t}\mathcal{F}\right] \\
&= -\iint \text{d}\mathcal{P}_1 \text{d}\Psi_0 \mathcal{G}\left[\frac{\partial}{\partial \mathcal{P}_1}\left(\mathcal{F}\frac{\text{d}\mathcal{P}_1}{\text{d}t}\right) + \frac{\partial}{\partial \Psi_0}\left(\mathcal{F}\frac{\text{d}\Psi_0}{\text{d}t}\right)\right] \\
&= \iint \text{d}\mathcal{P}_1 \text{d}\Psi_0 \mathcal{G}\frac{\partial}{\partial t}\mathcal{F} + \iint \text{d}\mathcal{P}_1 \text{d}\Psi_0 \mathcal{G}\frac{\partial}{\partial z}(\mathcal{F}v_z) \\
&= \frac{\partial}{\partial t}\iint \text{d}\mathcal{P}_1 \text{d}\Psi_0 \mathcal{G}\mathcal{F} + \frac{\partial}{\partial z}\iint \text{d}\mathcal{P}_1 \text{d}\Psi_0 \mathcal{G}\mathcal{F}v_z \\
&= \frac{\partial}{\partial t}\langle \mathcal{G}\rangle + \frac{\partial}{\partial z}\langle \mathcal{G}v_z\rangle.
\end{aligned} \qquad (11)$$

For the first three steps respectively, the chain rule, an integration by part and the continuity equation 10 have been used. With this relation, the system is reduced to a closed system of 3 equations for the two complex moments $\pi_1(\hat{z}, \tau)$, $\pi_2(\hat{z}, \tau)$ and the electric field envelope $F(\hat{z}, \tau)$:

$$\begin{cases}
\dfrac{\partial \pi_1}{\partial \tau} + \dfrac{\partial}{\partial \hat{z}}(\pi_1 \beta_z) = A_1 \pi_1 + i\tilde{C}_1 \pi_2 - \tilde{C}_2 C_0 F \\
\dfrac{\partial \pi_2}{\partial \tau} + \dfrac{\partial}{\partial \hat{z}}(\pi_2 \beta_z) = A_2 \pi_2 - i\tilde{C}_1 \pi_1 \\
\left(2i\dfrac{\partial}{\partial \tau} + \dfrac{\partial^2}{\partial \hat{z}^2} + \kappa_{\|0}^2\right)F = iC_3 C_0 \pi_1,
\end{cases} \qquad (12)$$

where $A_1 = i\tilde{\Delta}_0 + i\tilde{C}_1 + \beta_z\delta$ and $A_2 = i\tilde{\Delta}_0 - i\tilde{C}_1 + \beta_z\delta$. The boundary conditions for a gyrotron cavity are:

$$\pi_1(\hat{z}_{\text{in}}, \tau) = 0 \quad \pi_2(\hat{z}_{\text{in}}, \tau) = 0 \quad F(\hat{z}_{\text{in}}, \tau) = 0 \quad (13)$$

$$\left.\frac{dF}{d\hat{z}}\right|_{\hat{z}_{\text{out}}} = i\frac{k_\parallel}{k_0}F(\hat{z}_{\text{out}}, \tau). \quad (14)$$

The dimensionless constants are

$$\tilde{\Delta}_0 = 1 - \frac{s\Omega_c}{\gamma_0\omega_0}, \quad (15)$$

$$\tilde{C}_1 = \frac{p_{\perp 0}^2}{2s\gamma_0^2}, \quad (16)$$

$$\tilde{C}_2 = sp_{\perp 0}^{2s-2}, \quad (17)$$

$$C_3 = \frac{eZ_0}{m_e c^2 p_{z0}}\frac{I_b}{C_{mp}}\left(\frac{s^s}{2^s s!}\right)^2. \quad (18)$$

Finally, by Fourier transforming equations (12) in time, the partial differential equations (PDEs) can be rewritten as ordinary differential equations (ODEs). The Fourier transformation is done assuming $F \sim e^{-i\Omega\tau}$ and $\pi_{1,2} \sim e^{-i\Omega\tau}$, with $\Omega = (\omega - \omega_0)/\omega_0$ being the normalized difference between the rf-frequency ω and the reference frequency ω_0. The system of equations in its spectral form is given by:

$$\begin{cases} i\Omega\pi_1 = \dfrac{d}{d\hat{z}}(\pi_1\beta_z) - A_1\pi_1 - i\tilde{C}_1\pi_2 + \tilde{C}_2 C_0 F \\[2mm] i\Omega\pi_2 = \dfrac{d}{d\hat{z}}(\pi_2\beta_z) - A_2\pi_2 + i\tilde{C}_1\pi_1 \\[2mm] -2\Omega F = \dfrac{d^2 F}{d\hat{z}^2} + \kappa_{\parallel 0}^2 F - iC_3 C_0\pi_1. \end{cases} \quad (19)$$

This same set of equations could be used for studying beam-wave parasitic oscillations in smooth-wall beam-ducts with appropriate boundary conditions.

III. NUMERICAL IMPLEMENTATION

The equations are solved together as a general eigenvalue problem

$$A\mathbf{X} = \Omega B\mathbf{X}. \quad (20)$$

This is not a linear system, since the matrix A depends on the eigenvalue Ω, via the boundary conditions 14, as will be shown below. The real and imaginary parts of the eigenvalue Ω are respectively the frequency and the growth rate of the wave with $\text{Im}(\Omega) > 0$ for an unstable mode. The eigenvectors $\mathbf{X}$ are composed by the three complex fields $\pi_1(z)$, $\pi_2(z)$ and $F(z)$. The discretization in space is done using a finite difference scheme for the first and second order derivatives. It is expressed here for an equidistant discretization for more clarity ($\Delta\hat{z} = \hat{z}_i - \hat{z}_{i-1}, \forall i \in [2, N_z]$).:

$$\left.\frac{d\pi}{d\hat{z}}\right|_{i-\frac{1}{2}} \simeq \frac{\pi_i - \pi_{i-1}}{\Delta\hat{z}} \qquad \forall i = 1, ..., N_z. \quad (21)$$

Here, i and $i - 1$ are indices denoting points on the discretization grid and $i - \frac{1}{2}$ denotes a point centered between the two former points. N_z is the number of points. The second order spatial derivative is:

$$\left.\frac{d^2 F}{d\hat{z}^2}\right|_i \simeq \frac{F_{i+1} - 2F_i + F_{i-1}}{(\Delta\hat{z})^2} \qquad \forall i = 1, ..., N_z. \quad (22)$$

For an index $i \in]1, N_z[$, the two first equations of (19) become:

$$\pi_{1_{i-1}}\left(-\frac{\beta_z}{\Delta\hat{z}} + \frac{\beta_z'}{2} - \frac{A_1}{2}\right) + \pi_{1_i}\left(\frac{\beta_z}{\Delta\hat{z}} + \frac{\beta_z'}{2} - \frac{A_1}{2}\right) +$$
$$+ \pi_{2_{i-1}}\left(-\frac{i\tilde{C}_1}{2}\right) + \pi_{2_i}\left(-\frac{i\tilde{C}_1}{2}\right) +$$
$$+ F_{i-1}\left(\frac{\tilde{C}_2 C_0}{2}\right) + F_i\left(\frac{\tilde{C}_2 C_0}{2}\right) =$$
$$= \pi_{1_{i-1}}\left(\frac{i\Omega}{2}\right) + \pi_{1_i}\left(\frac{i\Omega}{2}\right), \quad (23)$$

and

$$\pi_{2_{i-1}}\left(-\frac{\beta_z}{\Delta\hat{z}} + \frac{\beta_z'}{2} - \frac{A_2}{2}\right) + \pi_{2_i}\left(\frac{\beta_z}{\Delta\hat{z}} + \frac{\beta_z'}{2} - \frac{A_2}{2}\right) +$$
$$+ \pi_{1_{i-1}}\left(\frac{i\tilde{C}_1}{2}\right) + \pi_{1_i}\left(\frac{i\tilde{C}_1}{2}\right) =$$
$$= \pi_{2_{i-1}}\left(\frac{i\Omega}{2}\right) + \pi_{2_i}\left(\frac{i\Omega}{2}\right), \quad (24)$$

where all the indices for the elements β_z, $\beta_z' = \frac{\partial\beta_z}{\partial\hat{z}}$, A_1, A_2, C_0, $\tilde{C}_1$ and $\tilde{C}_2$ have been omitted. Those elements are evaluated at $\hat{z}_{i-\frac{1}{2}}$. The third equation of 19 becomes:

$$F_{i-1} - F_i\left(2 - \Delta\hat{z}^2\kappa_{\parallel 0}^2\right) + F_{i+1} +$$
$$- \pi_{1_i}\left(i\Delta\hat{z}^2 C_3 C_0\right) = -2\Delta\hat{z}^2\Omega F_i. \quad (25)$$

Here, the elements $\kappa_{\parallel 0}$, C_0 and C_3 are evaluated at $\hat{z}_i$. The value of F_{N_z+1} is needed in the last wave-equation (25). It is expressed as function of F_{N_z} and F_{N_z-1}, using the radiation boundary condition (14):

$$F_{N_z+1} = 2i\Delta\hat{z}\frac{k_\parallel(\Omega)}{k_0}F_{N_z} + F_{N_z-1}. \quad (26)$$

An important point to be noted is that, in this expression, $k_\parallel$ depends on the eigenvalue Ω, and thus the operator A in (20) depends on the eigenvalue Ω. The boundary conditions at the entry (13) impose:

$$\pi_{1_1} = 0, \qquad \pi_{2_1} = 0, \qquad F_{1_1} = 0. \quad (27)$$

With this discretization, the eigenvalue problem (20) takes the form

$$\begin{pmatrix} A_{11} & A_{12} & A_{13} \\ A_{21} & A_{22} & 0 \\ A_{31} & 0 & A_{33}(\Omega) \end{pmatrix}\begin{pmatrix} \mathbf{\Pi_1} \\ \mathbf{\Pi_2} \\ \mathbf{F} \end{pmatrix} = \Omega\begin{pmatrix} B_{11} & 0 & 0 \\ 0 & B_{22} & 0 \\ 0 & 0 & B_{33} \end{pmatrix}\begin{pmatrix} \mathbf{\Pi_1} \\ \mathbf{\Pi_2} \\ \mathbf{F} \end{pmatrix}, \quad (28)$$

where $\mathbf{\Pi_1} = (\pi_{1_1}, \pi_{1_2}, ..., \pi_{1_{N_z}})$, $\mathbf{\Pi_2} = (\pi_{2_1}, \pi_{2_2}, ..., \pi_{2_{N_z}})$ and $\mathbf{F} = (F_1, F_2, ..., F_{N_z})$ are the three complex fields on a discretized vector form. The matrices A_{ij} contain at most three non zeros terms by row. Hence, sparse matrices are used to optimize numeric performance. Two methods have been tested to solve the eigenvalue problem. The first method, which will be retained, solves the problem using the Matlab[19] function *eigs*, which is based on routines from the *Arpack*[20] library. Since the very last term of the matrix A_{33} depends on the eigenvalue Ω, the eigenvalue problem is solved iteratively, starting for the first iteration with $\Omega = 0$, i.e. from the arbitrary reference frequency ω_0. The second method to solve the eigenvalue problem consists in searching the roots of $\det(A(\Omega) - \Omega B)$ using the Muller's method[21]. As this method uses quadratic interpolation, three initial guesses are needed. One iteration of the first method gives for example those three guesses. On figure 1 are reported the time needed by the two methods to perform 10 iterations, solving only the wave equation and for an equidistant discretization in the longitudinal direction z. The first method is faster for large N_z ($N_z > 600$), and thus for larger matrices. Moreover, by adding the time needed to compute the eigenvector in the second method, the first method is faster for $N_z > 400$. For this reason, the first method, calculating the eigenvalues with the Matlab script *eigs* has been retained.
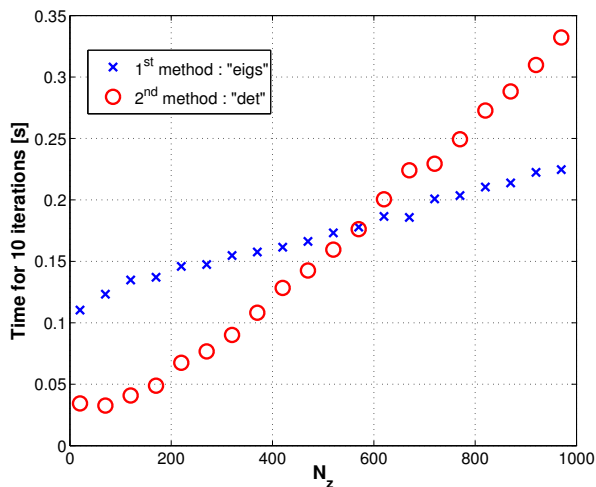

Figure 1. Time needed by the two methods to solve the eigenvalue problem with 10 iterations (average on 10 runs).

IV.   CODE DEVELOPMENT AND BENCHMARKING

A.   Validation against other codes

The cavity longitudinal profile used in the simulations is shown in figure 2 along with the external magnetic field and the electron beam position. This is the cavity of a 260 GHz gyrotron[17] used for DNP-NMR spectroscopy research.
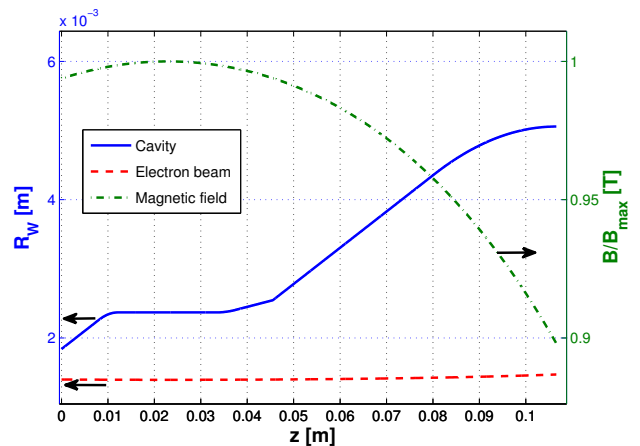

Figure 2. Longitudinal profile of the DNP-cavity (in blue), position of the electron-beam (in red, dashed) and normalized magnetic field profile (in green, dashed-dotted).

Code	Model	Num. implementation
Cavity (cold-cavity)	spectral	FEM
TWANGlin	temporal	FEM + RK
TWANGlinspec	spectral	FDM

Table I. Model and numerical implementation for the cold-cavity code "Cavity" and the time-evolution linear code "TWANGlin", both used to benchmark the new spectral code "TWANGlinspec". FEM, FDM and RK stand for Finite Element Method, Finite Difference Method and Runge-Kutta, respectively.

First of all, TWANGlinspec was tested without current ($I_b = 0$), i.e., without beam-wave interaction. It was benchmarked against the code Cavity, a cold-cavity code based on finite element method (see table I). For the comparison $N_z = 4225$ points for the discretization were chosen as well as 10 iterations in order to have a numerical convergence. The reference frequency ω_0 was set to the cutoff-frequency of the flat section of the cavity. The relative discrepancy between the first eigenvalue given by the two codes never exceeds 0.09% for both the real and imaginary parts. The discrepancies for higher modes are slightly larger, as expected, as a higher number of points is needed for the sampling (according to the Nyquist-Shannon sampling theorem).

A second validation step consisted in adding the self-consistent interaction with the electron beam. For this case, the comparison was done with the results of the code TWANGlin[6] (see table I). To solve the equations, the code TWANGlin uses a fourth order Runge-Kutta method for the two beam equations related to the moments π_1 and π_2 and a finite element method for the wave equation. In figure 3 are shown the real and imaginary

parts of the eigenvalues computed with the two codes, corresponding respectively to the frequency and growth rate of the wave, for different average step size $< dz >$ of the non-equidistant spatial discretization. The number of points N_z used for the discretization varies between 423 (far-right point) and 16897 (far-left point). As expected, the convergence is faster with the code TWANGlin, using a third order finite element method for the wave-equation, whereas a first order finite difference method is used in TWANGlinspec. In the following, at least 2000 points are considered for the discretization.
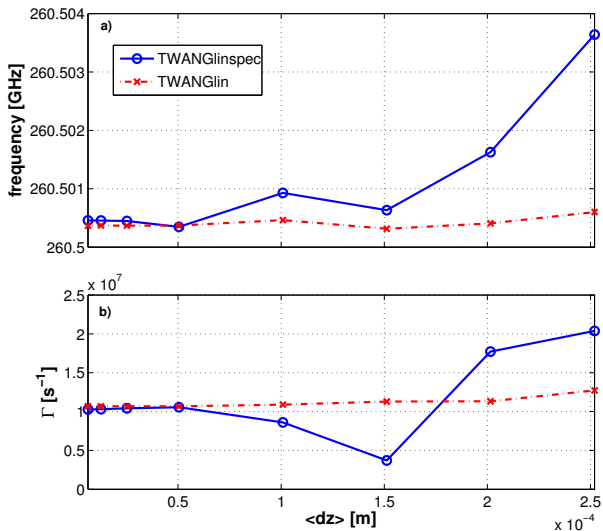
Figure 3. Frequency (a) and growth rate (b) versus the average step size $||dz||$ computed with the spectral code TWANGlinspec (in blue) and the time-dependent code TWANGlin.

B. Validation against experiments

The model in TWANGlinspec allows to consider real experimental system parameters with all the spatial inhomogeneities such as magnetic field or cavity radius inhomogeneities. An additional validation is done comparing the starting-current calculated with TWANGlinspec with experimental measurements. In gyrotrons, the starting current is the self excitation condition, i.e. a threshold current above which a mode is excited. The results of TWANGlinspec for the DNP-gyrotron[17] are presented in figure 4 along with experimental results. The simulation parameters are listed in the first part of table II. The agreement between TWANGlinspec and the experimental results is remarkably good over the whole range of magnetic field. With a time-dependent code, the calculation is also possible but requires long calculation, given the very small growth rate close to the starting current. With a spectral code, the calculation is faster, as it reduces to finding the root of the eigenvalue. Indeed, the

imaginary part of the eigenvalue Ω in (20) corresponds to the wave growth rate and the current, where this value becomes positive corresponds to the starting current.

Most of the start-up scenarios in gyrotron operations are based on non-self-consistent starting current calculation. The starting current of the analyzed DNP-gyrotron was calculated with such a fixed-field model and added in Fig. 4. A significant discrepancy is found between the correct starting current and the non-self consistent calculations, for example for magnetic field lower than 9.52T, corresponding to the positive detuning regime in which high-power gyrotrons are operated. A fully self-consistent model is thus preferable for start-up scenarios studies, as it has already been mentioned in several publications[6,8,10–13].

The TWANGlinspec code, based on a fully self-consistent model, is numerically efficient and allows to compute the starting current for a given transverse mode.
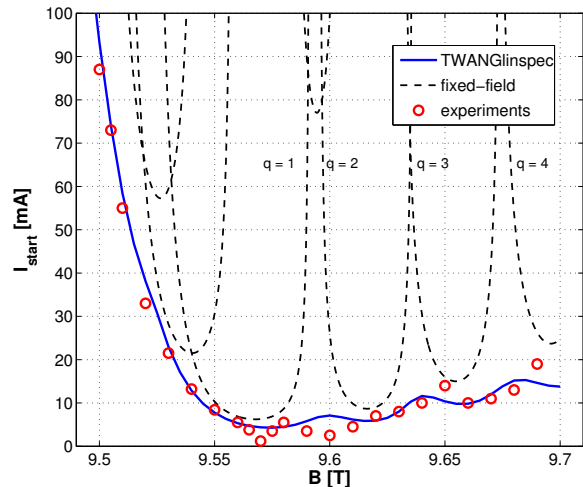

Figure 4. Starting current calculated with TWANGlinspec (in blue), with a fixed-field code (in black, dashed) and measured (red points).

V. RESULTS

In this section the model is applied to two different gyrotrons for which detailed experimental results have been obtained: a) DNP-gyrotron[17], already discussed earlier, characterized by a low-order high quality factor operating mode (low-power gyrotron) and b) a high-order low quality factor (high-power gyrotron) for which the experimental results are presented in the paper by Tax *et al.*[22].

Parameter	Value
Transverse mode	$TE_{7,2}$
Beam radius	1.394 mm
Pitch angle	1.9
Acceleration voltage	15.5 kV
Wall conductivity	$2.9 \cdot 10^7 \, S/m$
Magnetic field	9.55 T
Beam current	10 mA

Table II. Simulation parameters. The magnetic field, beam radius and pitch angle values are set in the middle of the constant radius section of the cavity.

A. DNP-gyrotron

As already mentioned, unlike time-dependent models, which describe the most unstable mode evolution, the spectral approach gives information on both stable, $Im(\Omega) < 0$, and unstable modes, $Im(\Omega) > 0$. This is illustrated in figure 5, for the simulation parameters given in table II. The horizontal axis represents the real part of the eigenvalues, corresponding to the wave frequency, whereas the vertical axis represents the imaginary part of the eigenvalues, corresponding to the wave growth rate. In this case, only one mode is unstable ($\Gamma > 0$). The field profiles corresponding to these eigenmodes are obtained via the eigenvector $\mathbf{X}$ in Eq.(20). The amplitude and phase of the electric field profile for the four modes highlighted in figure 5 are shown in figures 6 and 7. For the unstable mode, the electric field profile corresponds to the mode with one axial variation. The closest mode in the complex plane in figure 5 is the mode with two axial variations. By following the diagonal formed by these modes in the complex plane, all "usual" modes with increasing axial variations are found. On the other hand, all the modes situated in the bottom part of the complex plane, with $\Gamma < -2 \cdot 10^9 \, s^{-1}$, have their electric field profile mainly situated in the uptaper following the constant radius section of the cavity, as can be seen in figure 7. For the following, a distinction is made between the "usual" eigenmodes and these "uptaper" eigenmodes.

Analysis of the novel "uptaper" modes

With the above-described DNP gyrotron, non-stationary oscillations have been observed[17,18]. In a certain range of operating parameters, equidistant sidebands appear in the frequency spectrum. The "uptaper" modes show several similarities with these sidebands. First the "uptaper" modes, unlike the "usual" modes, are almost equidistant in frequency. Secondly, their electric field profiles are peaked in the uptaper. This has also been observed with the nonlinear code TWANG for sidebands with frequency lower than the cutoff frequency. The third similarity is the dependency on the pitch angle
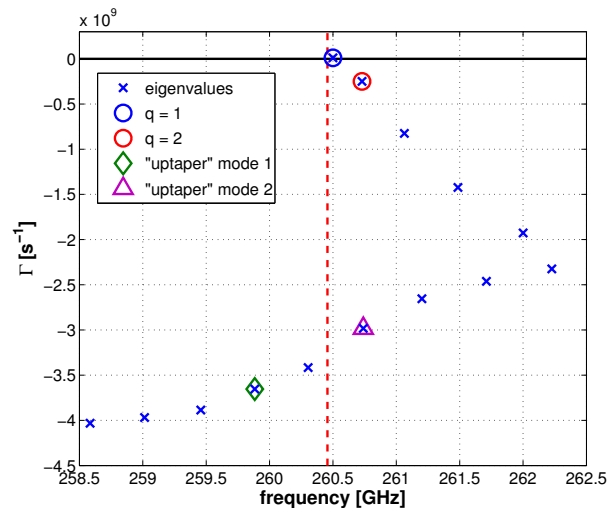

Figure 5. Real (frequency) and imaginary (growth rate) parts of the first 14 eigenvalues computed with TWANGlinspec. The dashed vertical red line indicates the cutoff frequency in the constant radius cavity part. The horizontal continuous black line indicates the limit between stable ($\Gamma < 0$) and unstable ($\Gamma > 0$) modes. The four symbols indicate which modes are considered in figures 6 and 7. (cf. table II for parameters).
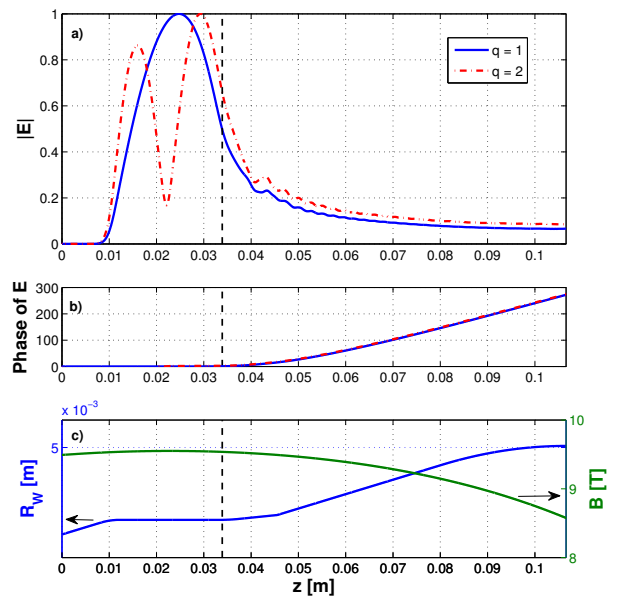

Figure 6. (a) and (b) Amplitude and phase of the electric field profile along the longitudinal direction, calculated with TWANGlinspec for two of the modes highlighted in figure 5. (c) Cavity and magnetic field profile. The dashed black line indicates the end of the cavity constant radius part. (cf. table II for parameters).
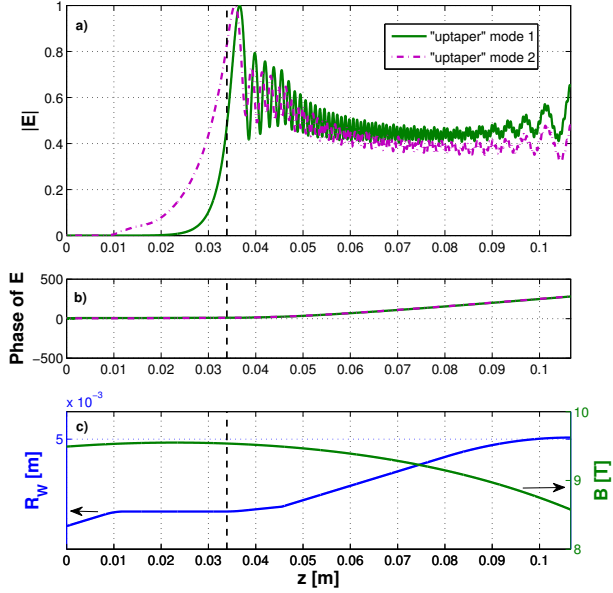
Figure 7. (a) and (b) Amplitude and phase of the electric field profile along the longitudinal direction, calculated with TWANGlinspec for two of the modes highlighted in figure 5. (c) Cavity and magnetic field profile. The dashed black line indicates the end of the cavity constant radius part. (cf. table II for parameters).

$\alpha = v_\perp/v_\parallel$. In the sideband regime, the frequencies in experiment are observed to fluctuate in time, while remaining equidistant at each moment, as can be seen in figure 9, which is a spectrogram acquired with an hetero-dyne system. It has been shown[18,23] that these frequency fluctuations are related to an anode voltage fluctuation, with the same periodicity and causing a modulation of the pitch angle. The sidebands are much more affected by this fluctuation than the main mode. The calculated eigenvalue spectrum for three values of the pitch angle, with a maximum relative difference similar to the experimental fluctuation ($\frac{\Delta\alpha}{\alpha} \approx 3\%$), is presented in figure 8. One observes that the "uptaper" modes are also much more affected than the "usual" modes, even though the absolute frequency difference is more important for the "uptaper" modes ($\Delta f \approx 150\,\text{MHz}$) than the maximum sidebands frequency modulation in the experiment ($\Delta f \approx 50\,\text{MHz}$).

These few observed similarities would suggest that these "uptaper" equidistant stable eigenmodes could be related to the experimentally observed equidistant side-bands. However, one should be careful while interpreting the results coming from the linear theory, given the fact that the sidebands occur in strongly nonlinear regimes. The mechanism that would lead to the excitation of these "uptaper" modes cannot be studied with this model and would require a nonlinear model adequate for studying non-stationary regimes such as TWANG-PIC[15].
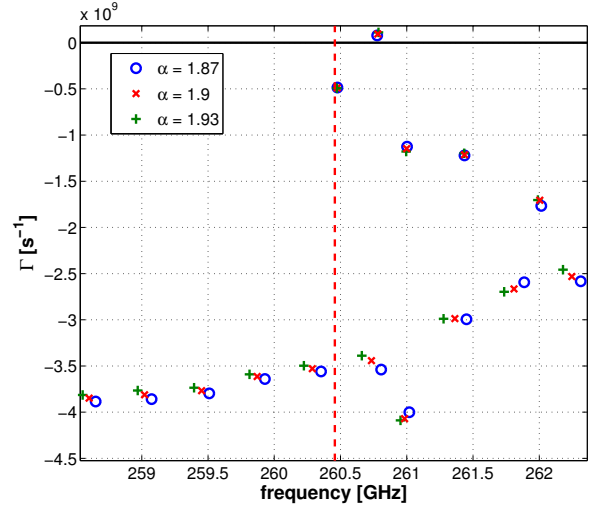

Figure 8. Real (frequency) and imaginary (growth rate) parts of the first 15 eigenvalues calculated for three different pitch angle values. (cf. table II for parameters, $B = 6.3\,\text{T}$).
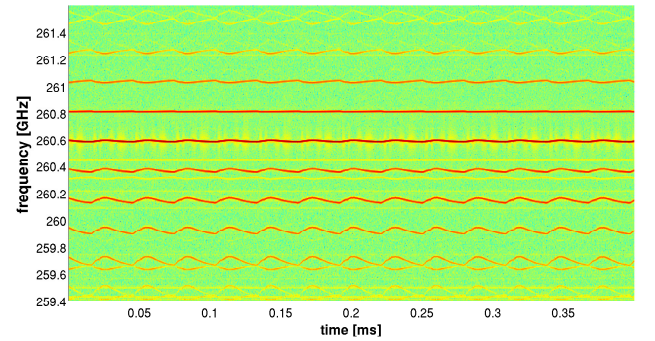

Figure 9. Spectrogram of experimental signal during non-stationary oscillation regime. The side-bands are more affected by the pitch angle fluctuations than the main mode.

B. MIT 110-GHz gyrotron

Another study has been carried out based on the experimental results obtained with the 1.5MW, 110 GHz MIT-gyrotron described in the paper by Tax *et al.*[22]. In the experimental results presented in this paper, it has been shown that during the start-up phase, a $\text{TE}_{21,6,4}$ mode is excited before the nominal $\text{TE}_{22,6,1}$ mode. For this study, the cavity profile and the parameters described in table III have been used. The system parameters of table III correspond to a specific time (t=1.45 microseconds) during the startup-phase described in Fig.3 of Tax's paper. Before considering the real magnetic field profile, an uniform magnetic field has been used for the starting current calculation. As the results for the two cases were significantly different, intermediate magnetic field profiles have been considered to study their effect on the starting current. Three of these different magnetic field

profile are presented in figure 10.

The starting current of the first longitudinal mode to be excited for the two transverse modes $TE_{21,6}$ and $TE_{22,6}$ are listed in table IV. For these parameters, all the modes correspond to backward-wave modes. With a constant magnetic field, the starting current of the $TE_{21,6,4}$ mode is lower than for the $TE_{22,6,3}$ mode, indicating that it is the mode which is excited first. This is in good agreement with what is observed experimentally[22]. On the contrary, with the intermediate, B_{int}, or real magnetic field profiles, B_{real}, shown in figure 10, the mode $TE_{21,6,q}$ has a larger starting current than the $TE_{22,6,q}$ mode. Even though the relative difference in magnetic field amplitude is only around 2% at the end of the simulated cavity region and lower than 0.2% until the end of the initial uptaper region, the starting current for the $TE_{21,6,3}$ mode is almost two times larger for the real magnetic field profile.

Another aspect to consider, in particular when such parameter sensitivity is observed, is the voltage depression associated to electron beam space charge. To assess this effect, based on the system parameters of III, a space-charge depression of $4\,kV$ has been calculated resulting in an electron beam kinetic energy of $E_b = 46\,kV$. The results for the two transverse modes using the real magnetic field profile are listed in table V. As it was the case for the different magnetic field profile, the results depend strongly on the accelerating voltage, especially for the $TE_{21,6}$ mode.

These two parameter studies illustrate that for start-up scenario studies, where reliable information on the starting current are needed, a precise knowledge on the experimental parameters is required. Finally, including the error bars on the system parameters one could account for any disagreement between theory and experiment.

Parameters	Value
Magnetic field maximum	4.38 T
Cathode voltage	50 kV
Pitch angle	0.7
Wall conductivity	$1.45 \cdot 10^7$ S/m
Beam radius	10.1 mm
Modes considered	$TE_{21,6}$ $TE_{22,6}$

Table III. Parameters used for the starting current calculations.

VI. CONCLUSION

A new self-consistent linear spectral code TWANGlinspec has been developed and extends the existing TWANG[6,14,15] series of codes. It has been implemented and validated against other codes. The model, taking into account the spatial inhomogeneities in the cavity geometry and in the magnetic field profile, and treating the ohmic wall losses self-consistently, is
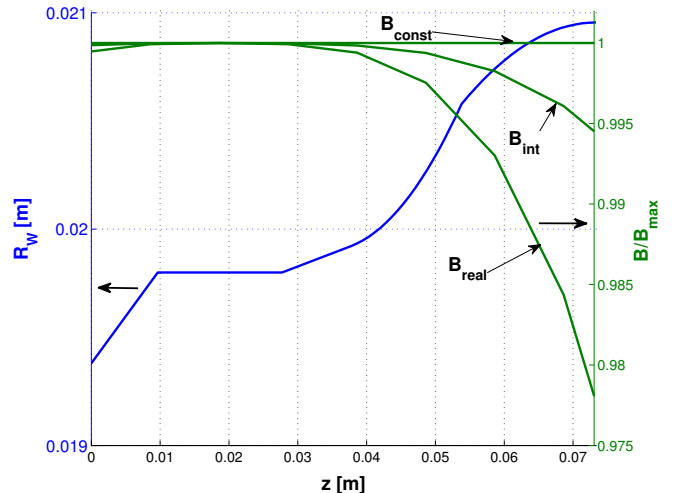

Figure 10. Longitudinal profile of the MIT 110 GHz cavity (in blue) and normalized magnetic field profiles used for the calculations (in green).

Mode	$I_{start}[A]$		
	B_{const}	B_{int}	B_{real}
$TE_{21,6,q}$	25.3 ($q=4$)	27 ($q=4$)	46.6 ($q=3$)
$TE_{22,6,q}$	27.1 ($q=3$)	26.8 ($q=2$)	29.5 ($q=1$)

Table IV. Starting current calculated with TWANGlinspec for the two transverse modes $TE_{21,6}$ and $TE_{22,6}$ and for the three different magnetic field profiles shown in figure 10. The assumed electron beam energy is $E_b = 50\,kV$. q indicates the longitudinal mode index of the mode.

Mode	$I_{start}[A]$	
	$E_b = 50\,kV$	$E_b = 46\,kV$
$TE_{21,6,q}$	46.6 ($q=3$)	31.7 ($q=4$)
$TE_{22,6,q}$	29.5 ($q=1$)	25.3 ($q=3$)

Table V. Starting currents calculated with TWANGlinspec for the two transverse modes $TE_{21,6}$ and $TE_{22,6}$ and for two different electron beam energy. The real magnetic field profile has been used for these calculations. q indicates the longitudinal mode index of the mode.

well adapted to describe a real experimental system. The agreement with experiment from a low power DNP-gyrotron is excellent and constitutes another benchmark for the code. Unlike the time-dependent approach, limited to the evolution of the most unstable mode, the spectral approach permits to get information on both stable and unstable eigenmodes. Consequently, a new set of equidistant stable eigenmodes has been identified, revealing similar parametric dependencies with respect to side-bands observed experimentally in a non-stationary regime. However, these non-stationary oscillations occur in strongly nonlinear regimes, and the mechanism that would lead to the excitation of the

"uptaper" modes cannot be studied with this linear model and is still under investigation. The new code is also convenient to calculate starting currents. Indeed, in the spectral formulation, the system takes the form of a general eigenvalue problem and the starting current calculation is done searching the current at which the imaginary part of the eigenvalue, corresponding to the growth rate, changes its sign. Compared to a time evolution approach, this approach leads to considerably shorter simulation time and is thus appropriate for parameter scans. Such a parameter study has been carried out with a high power gyrotron and revealed the importance of a precise knowledge on experimental parameters for start-up scenario studies. In the future, the code TWANGlinspec will be adapted to include a higher order discretization method for the wave equation. It will also be used to study spurious excitation of instabilities in beam-ducts[24–26], by adapting the boundary conditions and the wall losses with the corresponding impedance boundary conditions.

ACKNOWLEDGMENTS

REFERENCES

[1] A. W. Fliflet, M. E. Read, K. R. Chu, and R. Seeley. A self-consistent field theory for gyrotron oscillators: application to a low Q gyromonotron. *International Journal of Electronics*, 53(6):505–521, December 1982.

[2] K. R. Chu. The electron cyclotron maser. *Reviews of Modern Physics*, 76(2):489–540, May 2004.

[3] G. S Nusinovich. *Introduction to the physics of gyrotrons*. Johns Hopkins University Press, Baltimore, 2004.

[4] E. Borie and B. Jodicke. Comments on the linear theory of the gyrotron. *IEEE Transactions on Plasma Science*, 16(2):116–121, April 1988.

[5] Gregory S Nusinovich, Ruifeng Pu, Oleksandr V Sinitsyn, Jiao Yu, Thomas M Antonsen, and Victor L Granatstein. Self-Excitation of a Tapered Gyrotron Oscillator. *IEEE Transactions on Plasma Science*, 38(6):1200–1207, June 2010.

[6] F. Braunmueller, T. M. Tran, S. Alberti, J.-Ph Hogge, and M. Q. Tran. Moment-based, self-consistent linear analysis of gyrotron oscillators. *Physics of Plasmas*, 21(4):043105, April 2014.

[7] Gs Nusinovich. Linear-Theory of a Gyrotron with Weakly Tapered External Magnetic-Field. *International Journal of Electronics*, 64(1):127–135, January 1988. WOS:A1988L798400011.

[8] D. R. Whaley, M. Q. Tran, S. Alberti, T. M. Tran, Jr. Antonsen, T. M., and C. Tran. Startup Methods for Single-Mode Gyrotron Operation. *Physical Review Letters*, 75(7):1304–1307, August 1995.

[9] M. Yeddulla, G. S. Nusinovich, and T. M. Antonsen. Start currents in an overmoded gyrotron. *Physics of Plasmas*, 10(11):4513–4520, November 2003. WOS:000185989400037.

[10] Olgierd Dumbrajs, Toshitaka Idehara, Teruo Saito, and Yoshinori Tatematsu. Calculations of Starting Currents and Frequencies in Frequency-Tunable Gyrotrons. *Japanese Journal of Applied Physics*, 51(12):126601, December 2012.

[11] T. H. Chang, K. F. Pao, S. H. Chen, and K. R. Chu. Self-Consistent Effects on the Starting Current of Gyrotron Oscillators. *International Journal of Infrared and Millimeter Waves*, 24(9):1415–1420, September 2003.

[12] Gregory S. Nusinovich Eduard M. Khutoryan. Competition between modes with different axial structures in gyrotrons. *Physics of Plasmas*, 21(9), 2014.

[13] G. S. Nusinovich, M. Yeddulla, T. M. Antonsen, and A. N. Vlasov. Start-Up Scenario in Gyrotrons with a Nonstationary Microwave-Field Structure. *Physical Review Letters*, 96(12):125101, March 2006.

[14] S. Alberti, T. M. Tran, K. A. Avramides, F. Li, and J.-P. Hogge. Gyrotron parasitic-effects studies using the time-dependent self-consistent monomode code TWANG. *2011 36th International Conference on Infrared, Millimeter, and Terahertz Waves (irmmw-Thz)*, 2011.

[15] F. Braunmueller, T. M. Tran, Q. Vuillemin, S. Alberti, J. Genoud, J.-Ph Hogge, and M. Q. Tran. TWANG-PIC, a novel gyro-averaged one-dimensional particle-in-cell code for interpretation of gyrotron experiments. *Physics of Plasmas (1994-present)*, 22(6):063115, June 2015.

[16] S. Alberti, T. M. Tran, S. Brunner, F. Braunmueller, J. Genoud, J.-Ph Hogge, and M. Q. Tran. Generalized Radiation Boundary Conditions in Gyrotron Oscillator Modeling. *Journal of Infrared, Millimeter, and Terahertz Waves*, pages 1–16, September 2015.

[17] S. Alberti, J.-Ph Ansermet, K. A. Avramides, F. Braunmueller, P. Cuanillon, J. Dubray, D. Fasel, J.-Ph Hogge, A. Macor, E. de Rijk, M. da Silva, M. Q. Tran, T. M. Tran, and Q. Vuillemin. Experimental study from linear to chaotic regimes on a terahertz-frequency gyrotron oscillator. *Physics of Plasmas*, 19(12):123102, December 2012.

[18] S. Alberti, F. Braunmueller, T. M. Tran, J. Genoud, J-Ph. Hogge, M. Q. Tran, and J-Ph. Ansermet. Nanosecond Pulses in a THz Gyrotron Oscillator Operating in a Mode-Locked Self-Consistent Q-Switch Regime. *Physical Review Letters*, 111(20):205101, November 2013.

[19] Mathworks. MATLAB, 2013.

[20] D.C. Sorensen, R.B. Lehoucq, C. Yang, and K. Maschhoff. ARPACK - Arnoldi Package, 1996.

[21] William H. Press, Brian P. Flannery, Saul A. Teukolsky, and William T. Vetterling. *Numerical Recipes: The art of scientific computing.* Cambridge Univ. Press, 1986.

[22] D.S. Tax, O.V. Sinitsyn, W.C. Guss, G.S. Nusinovich, M.A. Shapiro, and R.J. Temkin. Experimental Study of the Start-Up Scenario of a 1.5-MW, 110-GHz Gyrotron. *IEEE Transactions on Plasma Science*, 41(4):862–871, April 2013.

[23] S. Alberti, F. Braunmller, T. M. Tran, J.-P. Hogge, J. Genoud, and M. Q. Tran. High-power THz-waves using gyrotrons: new physics results. *The 4th Shenzhen International Conference on Advanced Science and Technology*, 2013.

[24] Jiao Yu, Thomas M. Antonsen, and Gregory S. Nusinovich. Excitation of Backward Waves in Beam Tunnels of High-Power Gyrotrons. *IEEE Transactions on Plasma Science*, 38(6):1193–1199, June 2010.

[25] L. Thorndahl, S. Alberti, J.-P. Hogge, F. Li, and T.M. Tran. Comparative study of dielectric loaded structures for suppressing gyro-BWO instabilities in gyrotron beam-ducts (BD) using HFSS. In *2011 36th International Conference on Infrared, Millimeter and Terahertz Waves (IRMMW-THz)*, pages 1–3, Octo-

ber 2011.

[26]Guenter Dammertz Gerd Gantenbein. Experimental Investigations and Analysis of Parasitic RF Oscillations in High-Power Gyrotrons. *Plasma Science, IEEE Transactions on*, 38(6):1168 – 1177, 2010.